AGU PUBLICATIONS

JGR

Journal of Geophysical Research: Oceans

RESEARCH ARTICLE

10.1002/2016JC012091

Assessing recent air-sea freshwater flux changes using a surface temperature-salinity space framework

Jeremy P. Grist[1], Simon A. Josey[1], Jan D. Zika[2], Dafydd Gwyn Evans[3], and Nikolaos Skliris[3]

[1]National Oceanography Centre, University of Southampton, Southampton, UK, [2]Grantham Institute & Department of Physics, Imperial College London, London, UK, [3]Ocean and Earth Science, National Oceanography Centre Southampton, University of Southampton, Southampton, UK

Key Points:
- PME in T-S framework shows three distinctive cells of tropical (warm) P, subtropical E, mid-high latitude (cold) P
- All four atmospheric reanalyses show a strengthening of the water cycle between 1979 and 2007
- T-S framework shows that most of the increase in precipitation occurs in warm sector

Correspondence to:
J. P. Grist,
jeremy.grist@noc.ac.uk;
simon.a.josey@noc.ac.uk

Citation:
Grist, J. P., S. A. Josey, J. D. Zika, D. G. Evans, and N. Skliris (2016), Assessing recent air-sea freshwater flux changes using a surface temperature-salinity space framework, *J. Geophys. Res. Oceans*, *121*, 8787–8806, doi:10.1002/2016JC012091.

Received 24 JUN 2016
Accepted 4 NOV 2016
Accepted article online 11 NOV 2016
Published online 19 DEC 2016

Abstract A novel assessment of recent changes in air-sea freshwater fluxes has been conducted using a surface temperature-salinity framework applied to four atmospheric reanalyses. Viewed in the T-S space of the ocean surface, the complex pattern of the longitude-latitude space mean global Precipitation minus Evaporation (PME) reduces to three distinct regions. The analysis is conducted for the period 1979–2007 for which there is most evidence for a broadening of the (atmospheric) tropical belt. All four of the reanalyses display an increase in strength of the water cycle. The range of increase is between 2% and 30% over the period analyzed, with an average of 14%. Considering the average across the reanalyses, the water cycle changes are dominated by changes in tropical as opposed to mid-high latitude precipitation. The increases in the water cycle strength, are consistent in sign, but larger than in a 1% greenhouse gas run of the HadGEM3 climate model. In the model a shift of the precipitation/evaporation cells to higher temperatures is more evident, due to the much stronger global warming signal. The observed changes in freshwater fluxes appear to be reflected in changes in the T-S distribution of the Global Ocean. Specifically, across the diverse range of atmospheric reanalyses considered here, there was an acceleration of the hydrological cycle during 1979–2007 which led to a broadening of the ocean's salinity distribution. Finally, although the reanalyses indicate that the warm temperature tropical precipitation dominated water cycle change, ocean observations suggest that ocean processes redistributed the freshening to lower ocean temperatures.

1. Introduction

Variations in the air-sea fluxes of heat and freshwater are an important influence on water mass properties and ocean circulation on multiple time and space scales. Since the 1950s, spatially coherent positive near-surface salinity trends exceeding 0.2 pss/50 years have been observed in many evaporation-dominated regions such as the subtropical gyres of all three major oceanic basins. In turn, decreasing salinity trends exceeding −0.2 pss/50 years are found in precipitation-dominated regions such as the Western Pacific Warm Pool and the North Pacific subpolar region [e.g., *Durack and Wijffels*, 2010; *Skliris et al*., 2014]. These patterns are consistent with expected surface freshwater flux changes associated with intensification of the global hydrological cycle. Such changes are predicted by climate models [*Held and Soden*, 2006; *Durack et al*., 2012] but have proved hard to confirm from observations due to the difficulty in obtaining sufficiently accurate precipitation and evaporation data sets over much of the global ocean. At regional scales, freshwater flux variations contributed significantly to North Atlantic eastern subpolar gyre freshening from the mid-1970s to 1990s [*Josey and Marsh*, 2005].

With regard to recent trends in the precipitation component of the surface freshwater flux, *Allan et al*. [2010] used data from the Global Precipitation Climatology Project (GPCP) to analyze tropical precipitation trends. The GPCP data set consists of precipitation estimates derived from a synthesis of infra-red radiances and rain gauges since 1979 with microwave ocean measurements from Special Sensor Microwave Imager (SSM/I) since 1988. *Allan et al*. [2010] found that precipitation over the wettest 30% of the tropical Oceans increased by 1.8%/decade between 1979 and 2008 while, over the driest 30%, precipitation decreased by 2.6%/decade. These findings were consistent with those of *Adler et al*. [2008] who found precipitation increased by 0.06 mm/decade over the tropical oceans between 1979 and 2006 using the same data set. For different subsets of the satellite era, *Wentz et al*. [2007] and *Gu et al*. [2016] also found significant increases in tropical precipitation, particularly in the Pacific warm pool.

With regard to the evaporation component of the freshwater flux, a study using the Objectively Analyzed Air–Sea Fluxes (OAFlux) found evaporation increasing between the 1990s and the 1970s particularly in western boundary currents and the Indo-Pacific Tropical Warm pool [*Yu*, 2007]. The same study also found a slight decrease in the evaporation over the subtropical regions where there are maxima in net evaporation. The trend patterns for 1977–2006 found in the tropical and subtropical Pacific by *Li et al*. [2011] were also consistent with this picture. More recently, *Gao et al*. [2013] examined latent heat flux trends between 1988 and 2008 using the Goddard Satellite-based Surface Turbulent Fluxes version 2c (GSSTF2c). They found particularly strong ($\sim$10 Wm^{-2}/decade) trends over the western boundary currents but also in the subtropics of the southern hemisphere.

Most of the aforementioned studies examine air-sea freshwater flux variability in geographical coordinates. In this study we take an alternative approach of examining air-sea flux variability in temperature-salinity (T-S) space. The advantage of such an approach is that it provides a more physically instructive link to water mass transformation processes and changes in the global thermohaline circulation. Specifically, in this study, changes in surface fluxes are related to changes in the T-S distribution. We consider air-sea flux variability in four diverse atmospheric reanalyses (NCEP2, JRA, MERRA and ERA-Interim, described previously by *Grist et al*. [2014]) and highlight the results that are most robust across these products. To define the T-S space of the surface ocean we use surface fields from the EN4 gridded potential temperature and salinity data set [*Good et al*., 2013].

The structure of this paper is as follows. The methodology used in the study is described in section 2, while the observations and the model output to which the method is applied are described in section 3. In section 4, results of an examination of the surface freshwater variability and its impact on the ocean are presented. Finally, in section 5 a summary and conclusions are presented.

2. Methodology

The following two stages of analysis have been applied to both observations and the climate model output detailed in section 3.

2.1. Analysis of Surface Fluxes in Temperature-Salinity Space

For each month, the total precipitation, P, minus evaporation, E, falling into discrete temperature-salinity bins, Precipitation minus Evaporation (PME), was calculated via

$$\mathrm{PME}(\mathrm{T},\mathrm{S}) \;=\; \frac{1}{\Delta S \Delta T}\int\int \Pi\left(\pm\frac{\Delta T}{2},\pm\frac{\Delta S}{2}\right)(P-E)dA \tag{1}$$

where $\Pi\left(\pm\frac{\Delta T}{2},\pm\frac{\Delta S}{2}\right)$ is a boxcar function equaling 1 within $\pm\frac{\Delta T}{2}$ of T and $\pm\frac{\Delta S}{2}$ of S and 0 elsewhere and $\iint dA$ is an integral over the ocean surface. The dimensions of the bins were 1°C in temperature and 0.2 pss in salinity. PME has units of m^3 per s, °C and pss so that it does not scale with bin size. Once these monthly PME(T,S) fields had been calculated they were converted to annual means. The linear trend associated with the 29 annual fields over the 1979–2007 observational period was then calculated. For the case of the model analysis the annual PME(T,S) values were calculated directly from annual averaged (latitude-longitude) PME and surface temperature and salinity fields using (1). In order to put observed changes into context of the type of changes associated with anthropogenic global warming on the same and longer time scales, annual trends from the climate model were calculated for (a) the 29 year period representative of present day and for (b) a 140 year period representative of century scale climate change.

2.2. Analysis of Volumetric Temperature-Salinity Changes and Inferred Water Transformation.

The change in the amount of water within temperature and salinity bins is used to estimate dia-thermal and dia-haline transformations following the approach of *Evans et al*. [2014] and summarized here.

Let $V(T,S)$ be the total volume of water over a discrete temperature, ΔT, and salinity interval, ΔS, in the global ocean. In the absence of compressible effects, this volume can only change if there is some water mass transformation causing water to cross either isotherms ($G_T(T,S)$; the amount of water transforming from low to high temperature over a salinity interval ΔS) or isohalines ($G_S(T,S)$; the amount of water transforming from low to high salinity over a temperature interval ΔT) and through the addition of water at the sea

surface. Our analysis of global PME and T-S fields indicates that the volume change of a T-S bin by the addition of water at the surface is a small contribution to the total change in $V(T,S)$ (the rms is less than 1%). Therefore the influence of the direct addition of water is neglected. Note that fresh water fluxes still change sea water salinity and hence transform water from one T-S bin to another. In this way the fresh water flux is approximated as an equivalent salt flux as is customary in many ocean models. More precisely, V is related to the convergence of diahaline (G_S) and diathermal (G_T) transformations

$$\frac{dV}{dt} = [G_T]_{T-\Delta T/2,S}^{T+\Delta T/2,S} + [G_S]_{T,\ S-\Delta S/2}^{T,\ S+\Delta S/2} \tag{2}$$

See *Hieronymus et al*. [2014] for the continuous form of (2) and its derivation. The transformation rates, G_T and G_S, are only possible if there is some convergence of heat and salt due to surface fluxes and mixing such that, in the case of salinity

$$G_S(T,S) \approx \frac{1}{\Delta S}\int\int \Pi\left(\pm\frac{\Delta T}{2}, \pm\frac{\Delta S}{2}\right) S_0 f_w dA + \frac{1}{\Delta S}\int\int\int \Pi\left(\pm\frac{\Delta T}{2}, \pm\frac{\Delta S}{2}\right) \nabla\cdot \boldsymbol{K}\nabla S dV \tag{3}$$

where $\int\int\int dV$ is an integral of the entire volume of the ocean, an equivalent salt flux is approximated by multiplying the fresh water flux, f_w, per unit area by a reference salinity S_0, and $\boldsymbol{K}$ is a diffusion tensor. Note that via the divergence theorem the mixing term in (3) can also be represented as an integral of the diffusive flux across the four interfaces that bound the volume. In the absence of changes in mixing, river run off and ice melt, changes in the saline transformation rate, G_S', are directly related to the changes in the fresh water flux, PME′, such that $\mathrm{PME}' = G_S'/S_0\Delta T$.

Given only dV/dt, there are infinite solutions for G_S and G_T which satisfy (2). Even where dV/dt = 0, G_S and G_T are nonzero and define a steady thermohaline circulation [e.g., *Zika et al*., 2012; *Groeskamp et al*., 2014]. We choose to find a solution for the smallest transformation anomalies G_S' and G_T' which satisfy (2). This is done by setting G_S' and G_T' to zero where $V = 0$ (excluding solutions where transformation occurs within water masses that have not been observed) and minimizing $\mathrm{rms}(G_T) + \mathrm{rms}(G_S)$ globally via least squares. This therefore represents the minimum water mass transformation required to explain a given trend in V.

Using the same approach and the same temperature and salinity bins as in section 2.1, annual fields of (i) surface area of the global ocean, (ii) the volume of the global ocean in the top 100 m and (iii) the volume of the global ocean for the full depth of the ocean, that fall within each of the T-S bins were calculated. Trends were also calculated in the same way as in section 2.1.

3. Atmospheric Reanalysis, Model Data, and Model Output

3.1. Atmospheric Reanalysis Surface Freshwater Fluxes

Estimates of air-sea fluxes of freshwater are taken from four atmospheric reanalysis products that span 1979–2007. Key characteristics and references for the products are listed in Table 1. In each case, historical, quality-controlled atmospheric and surface data are assimilated into a Numerical Weather Prediction (NWP) Model. Throughout the 29 year period covered, the assimilation schemes and model stay constant, but the number of available observations vary. Details of the reanalysis-specific assimilation schemes are found within the references in Table 1.The specific fields used in the study are precipitation (P) and evaporation

Table 1. Summary of Atmospheric Reanalysis Products Used to Provide PME for This Study

Data Set	Abbreviation	Prescribed SST Field	Time Span Used	Approximate Horizontal Resolution	Reference
Japanese 25 year Reanalysis (JRA-25)/JMA Climate Data Assimilation System:	JRA	*Ishii et al*. [2005]	1979–2007	1.125° ×1.125°	*Onogi et al* [2007]
NCEP/DOE Reanalysis II	NCEP2	*Taylor et al*. [2000]	1979–2011	1.875° × 1.915°	*Kanamitsu et al*. [2002]
ECMWF Interim Reanalysis	ERA-I	Before 2002: *Fiorino* [2004] 2002 onward the operational forecast system [see *Dee et al*., 2011]	1979–2011	1.500° × 1.500°	*Dee et al*. [2011]
NASA Modern Era Reanalysis for Research and Applications	MERRA	*Reynolds et al*. [2002]	1979–2011	0.667° ×0.500°	*Rienecker et al*. [2011]

(E), from which surface net precipitation (PME, units m s^{-1}) is obtained. We note that precipitation is a model output not constrained by precipitation data itself, but by the other assimilated observations and the physics and dynamics of the model. However, all reanalysis variables, regardless of the extent they are constrained by observations form part of the internally consistent reanalysis product. The analysis is carried out for the period January 1979 to December 2007 which is used to calculate means and departure from means, standard deviations and linear trends. This period is chosen because studies suggest that during this time changes in the tropical atmospheric circulation (weakening of the Walker cell and a widening of the tropical belt) consistent with a global warming signal have been observed [e.g., *Seidel et al*., 2008].

3.2. Salinity and Temperature Data

In order to assign the surface fluxes into temperature-salinity (hereafter T-S) space, salinity and potential temperature fields are taken from the surface level of EN4 [*Good et al*., 2013] global 1° gridded product (version EN4.1.1 with *Gouretski and Reseghetti* [2010] corrections). EN4 and its predecessor EN3 have been used in numerous studies of decadal scale variability of water mass characteristics [e.g., *Skliris et al*., 2014; *Zika et al*., 2015]. The original sources of the profiles include the World Ocean Database (2005), the Global Temperature–Salinity Profile Programme (from 1990) and profiling float data from the Argo Global Data Assembly Center (from 1999). We utilize the monthly data from January 1979 to December 2007. In order to calculate water mass volume trends for the top 100m and the full depth, the same data set was utilized.

3.3. The HadGEM3 Coupled Climate Model

This study utilizes the GC2 configuration [*Williams et al*., 2015] of the state of the art climate model HadGEM3 [*Hewitt et al*., 2011], which is now introduced. HadGEM3 has been used in a number of climate studies including an examination of the impact of a shutdown of the Atlantic Meridional Overturning Circulation [*Jackson et al*., 2015]. Here we utilized the 1% per annum increase in CO_2 projection (hereafter H1PC) along with the companion fixed present day CO_2 concentration control run (hereafter Hctrl), both of 140 years duration. Further details of these runs are described in *Senior et al*. [2016]. Detailed descriptions of the model are found in *Williams et al*. [2015], *Hewitt et al*. [2011], and *Jackson et al*. [2015], here we focus on describing the model resolution and the significance of the improvements relative to previous version of the model [*HadGEM2 Development Team*, 2011]. The atmosphere model is version Global Atmosphere vn6.0 of the Met Office unified model with a horizontal resolution of N216 (approximately 60 km in midlatitudes) and 85 vertical levels. The improved horizontal resolution facilitates a more realistic description of midlatitude jet stream variability. The improved vertical resolution is particularly focused on the stratosphere with the aim of improving the representation of teleconnections [*Ineson and Scaife*, 2009].

The ocean model is the Global Ocean 5 (GO5) [*Megann et al*., 2013] version of the ORCA025 configuration of the NEMO model [*Madec*, 2008] with a nominal horizontal resolution of 0.25°. Because of the increased horizontal resolution the model no longer uses the GM [*Gent and McWilliams*, 1990] parameterization for horizontal eddy mixing of tracers. The ocean model has 75 model levels with a thickness of 1m at the surface increasing to approximately 200 m at a depth of 6000 m. The increased horizontal resolution in the ocean improves the position of the Gulf Stream, reducing the extent of the preexisting North Atlantic cold bias [*Scaife et al*., 2011]. The increased vertical ocean resolution is designed to improve the representation of the diurnal cycle [*Bernie et al*., 2008].

The sea ice model is version 4.1 of the Los Alamos National Laboratory sea ice model, CICE [*Hunke and Lipscomb*, 2010] and has the same resolution as the ocean model.

4. Results

4.1. Changes in PME

Mean PME fields for the four reanalyses are shown in Figures 1a, 1c, 1e, and 1g and in T-S space in panels b, d, f and h. Viewed in latitude-longitude space the PME field has a high degree of structure. In T-S space, this structure reduces to three distinct regions demonstrating the advantage of our approach in particular for relating PME to changes in global water mass characteristics. First, there is a tropical net precipitation belt, associated with the Intertropical Convergence Zone, the South Pacific Convergence Zone and the high net precipitation areas over the Bay of Bengal and the Maritime Continent. This region occupies the relatively large salinity range between 33 and 35.5 pss and a temperature range approximately between 28 and 31°C.

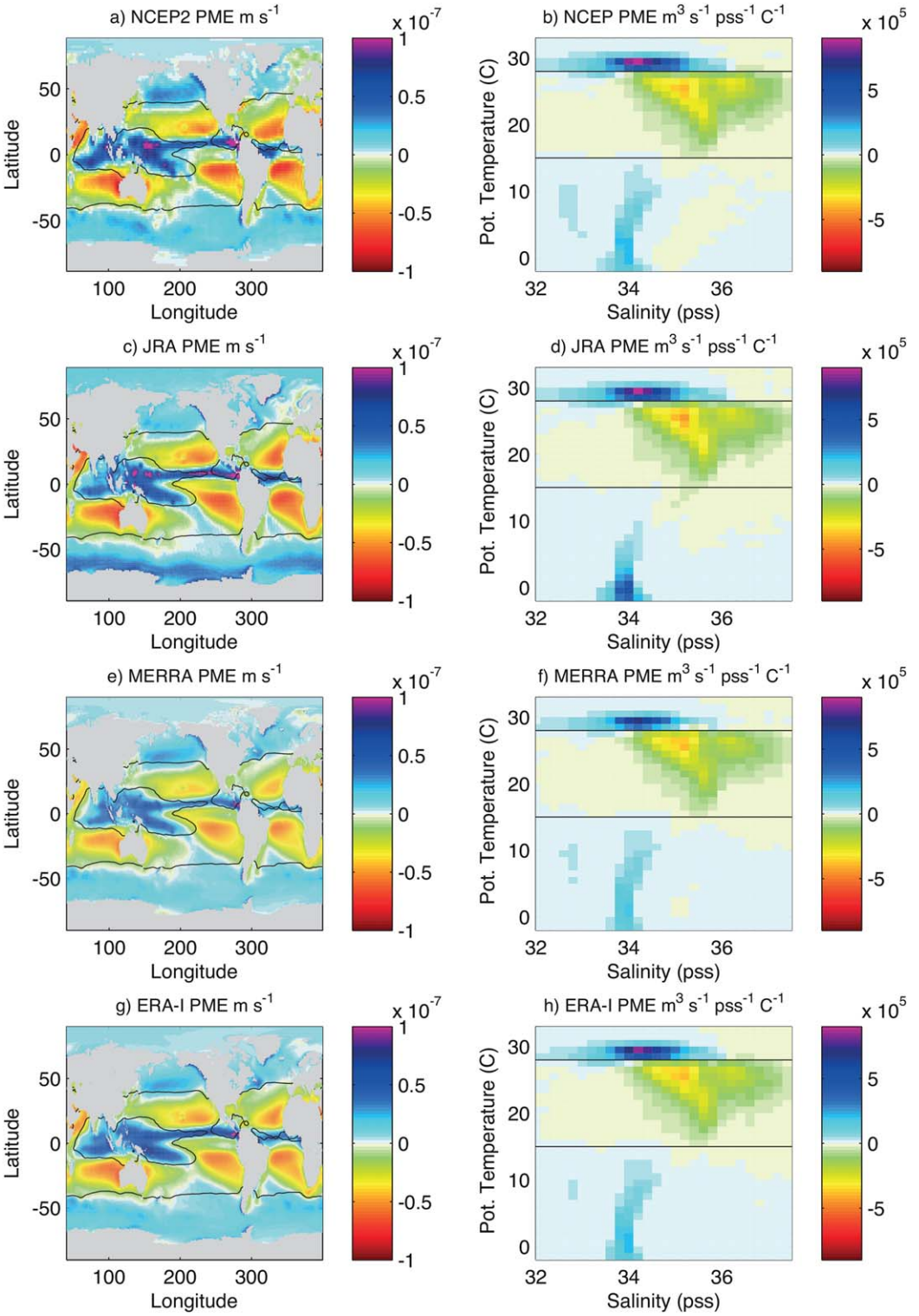

Figure 1. Mean PME (m s^{-1}) for 1979–2007 from (a) NCEP2; (c) JRA; (e) MERRA, and (g) ERA-I reanalyses and (b, d, f, and h) for T-S space (1°C temperature bins and 0.2 pss salinity bins, units are m^3 s^{-1} C^{-1} pss^{-1}), respectively. Black lines denote the 15°C and 28°C contours which approximately delineate the subtropical net evaporative zone from the tropical and middle-high latitude net precipitation zones.

The second band, associated with net evaporation over the subtropics covers the largest salinity range from 34.2 pss to 37 pss at its high temperature limit, 28°C. At its low temperature limit (17°C), the subtropical band is confined between 35.5 and 36 pss. Third, there is a region associated with mid-high latitude net

precipitation. The strongest net precipitation of this region occurs between −1°C to 8°C and 33.8–34.2 pss. However from this central region, there are two further spurs. The first spur is at the lowest temperature (between −1° C and 0°C) where the salinity range is extended to cover between 33.6 pss and 34.4 pss. The second encompasses the region from 8°C to 11°C and from 34.0 to 34.6 pss. In the mean state, there is broad agreement between the reanalyses with regard to the distribution of PME in both geographical and T-S coordinates.

The 1979–2007 linear trends in PME in T-S space from the 4 reanalyses are examined in Figure 2. In the figure, grey and black dots denote where half the change between 1979 and 2007 associated with a linear trend is greater than 1.5 and 2 times the standard deviations of the de-trended time series respectively. This same measure of trend significance is used throughout. Three (NCEP2, JRA, MERRA) of the four reanalyses show strong and significant net precipitation increases in the 28°–32° C tropical region. The largest trend being recorded in the fresher part of the belt, between 33.0 and 34.5 pss (which corresponds to the eastern tropical Pacific). Even though the ERA-I reanalysis has a markedly different trend in tropical net precipitation, with a broad region of decreasing net precipitation at salinities greater than 34.2 pss, it still shows increasing net precipitation near 34.0 pss and 32°C in common with the other reanalyses. As well as an increase in tropical net precipitation, there are also significant changes in net precipitation in the mid-high latitude band. NCEP2 and MERRA show a significant increase in net precipitation at salinities less than 34.0 and temperatures less than 10 °C, while JRA and ERA-I show a decrease in net precipitation at salinities greater than 34.0. Considering the mean trends of all the four reanalysis products (Figure 2e), it is seen that the increase in precipitation at lower salinities is a robust feature in the tropical belt and to a lesser extent also emerges at the high latitudes (−2 to 6°C). A noticeable, but less robust feature is an increase in net evaporation over the fresher parts of the subtropical evaporation cell. Finally, there is little agreement in the reanalysis trends at high salinities (greater than 34.5pss) in the tropics.

We have shown that the trends described above are robust across multiple reanalyses. However, it should be noted that the temporally varying observing network may result in time dependent biases with the potential to introduce unphysical trends [*Fasullo*, 2012; *Robertson et al*., 2011]. In particular, prior to the introduction of the Special Sensor Microwave Imager (SSM/I) in 1987, the first decade of the period (1979–2007) considered is relatively sparse in assimilated satellite data compared to thereafter. To address this concern, we have recomputed the trends using the subperiod 1989–2007 (see Figure 3). There are some minor differences in the trend patterns between the two periods in particular the reduced trend in JRA between the 5°C and 13°C temperature range. However, the overall level of consensus is strong and the resulting composite pattern shows the main features expected from an amplification of the water cycle. Hence, use of data from 1979 onward has not strongly influenced our results.

Before moving to discuss the results from the climate model we separately consider PME in the Atlantic basin and the combined Indian and Pacific Basin (Figure 4). In Figures 4a and 4b are the mean PME for the two respective basins. For orientation the same contours used in Figure 2e are used to indicate the location of the global precipitation and evaporation cells. Figures 4a and 4b demonstrate that the Atlantic PME cells occupy a higher salinity range, particular in the tropics and subtropics. It is also evident that, both in terms of the mean and the trend (Figures 4c and 4d), the Atlantic is a relatively small part of the Global PME when partitioned into T-S coordinates. Nevertheless, the individual basins do display features that are consistent with a tendency for fresh regions to become fresher and saline regions to increase salinity. In the Atlantic the precipitation increases in the warm (> 28 °C) net precipitation region and evaporation increases in the most saline part of the net evaporative subtropical region (37 pss, 20–25°C). While in the Indo-Pacific, net precipitation increases in the fresher part (<34 pss) and decreases in the more saline part of the warm net precipitation region. Net evaporation increases in the subtropical net evaporation region (34. 36.5 pss, 18–26°C).

The atmospheric reanalysis trends for 1979–2007 will now be put into context of the trends associated with global warming. Specifically we examine the trend in (a) the first 29 years and (b) the first 140 years of run H1PC. The same quantities are also calculated for Hctrl to provide an indication of the changes that are associated with model drift as opposed to greenhouse gas induced changes. The mean PME in HadGEM3 (Figures 5a and 5b) has a similar magnitude and spatial distribution to the atmospheric reanalysis. However a noticeable difference is that the high latitude precipitation cell is centered at higher temperature (from 0 to 17°C) in H1PC. The warmer (and to a certain extent fresher) locations of the cells reflect the warmer mean surface ocean conditions in H1PC. The 29 year trend in H1PC (Figure 5c) displays some similarities to

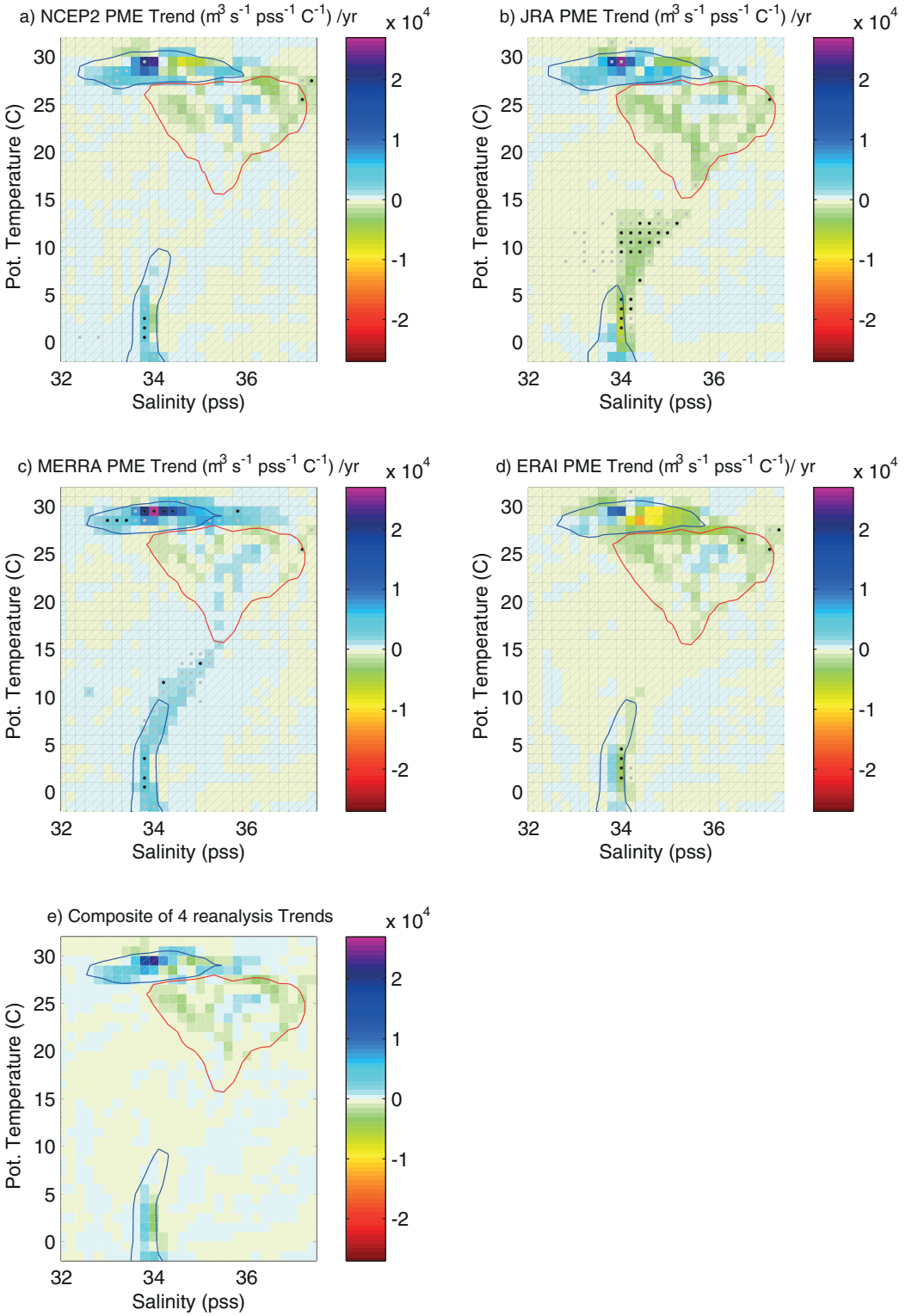

Figure 2. PME ($m^3\ s^{-1}\ pss^{-1}\ C^{-1}$/yr) trends (1979–2007) in TS space from the (a) NCEP2; (b) JRA, (c) MERRA, and (d) ERAI atmospheric reanalysis. Grey and black dots denote where half the change between 1979 and 2007 associated with a linear trend is greater than 1.5 and 2 times the standard deviations of the de-trended time series respectively. (e) Composite of the four reanalyses trends. The mean positions of the main net precipitation and net evaporation cells (as defined by the positive and negative mean $0.5 \times 10^5\ m^3\ s^{-1}\ pss^{-1}\ C^{-1}$ contours) are shown as blue and red contours respectively.

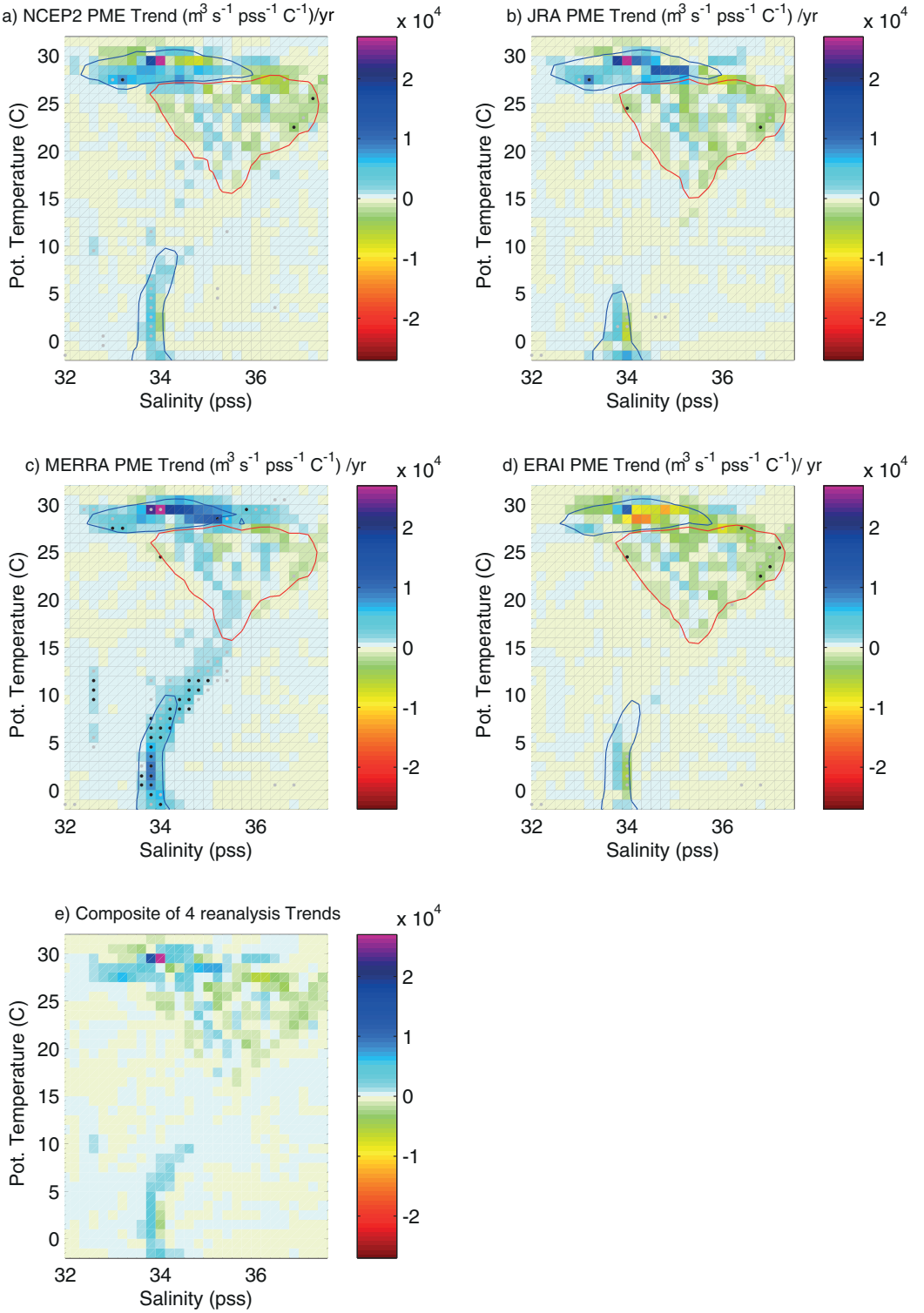

Figure 3. PME ($m^3\ s^{-1}\ pss^{-1}\ C^{-1}$/yr) trends (1989–2007) in TS space from the (a) NCEP2, (b) JRA, (c) MERRA, and (d) ERAI atmospheric reanalysis. Grey and black dots denote where half the change between 1989 and 2007 associated with a linear trend is greater than 1.5 and 2 times the standard deviations of the de-trended time series respectively. (e) Composite of the four reanalyses trends. The mean positions of the main net precipitation and net evaporation cells (as defined by the positive and negative mean $0.5 \times 10^5\ m^3\ s^{-1}\ pss^{-1}\ C^{-1}$ contours) are shown as blue and red contours respectively.

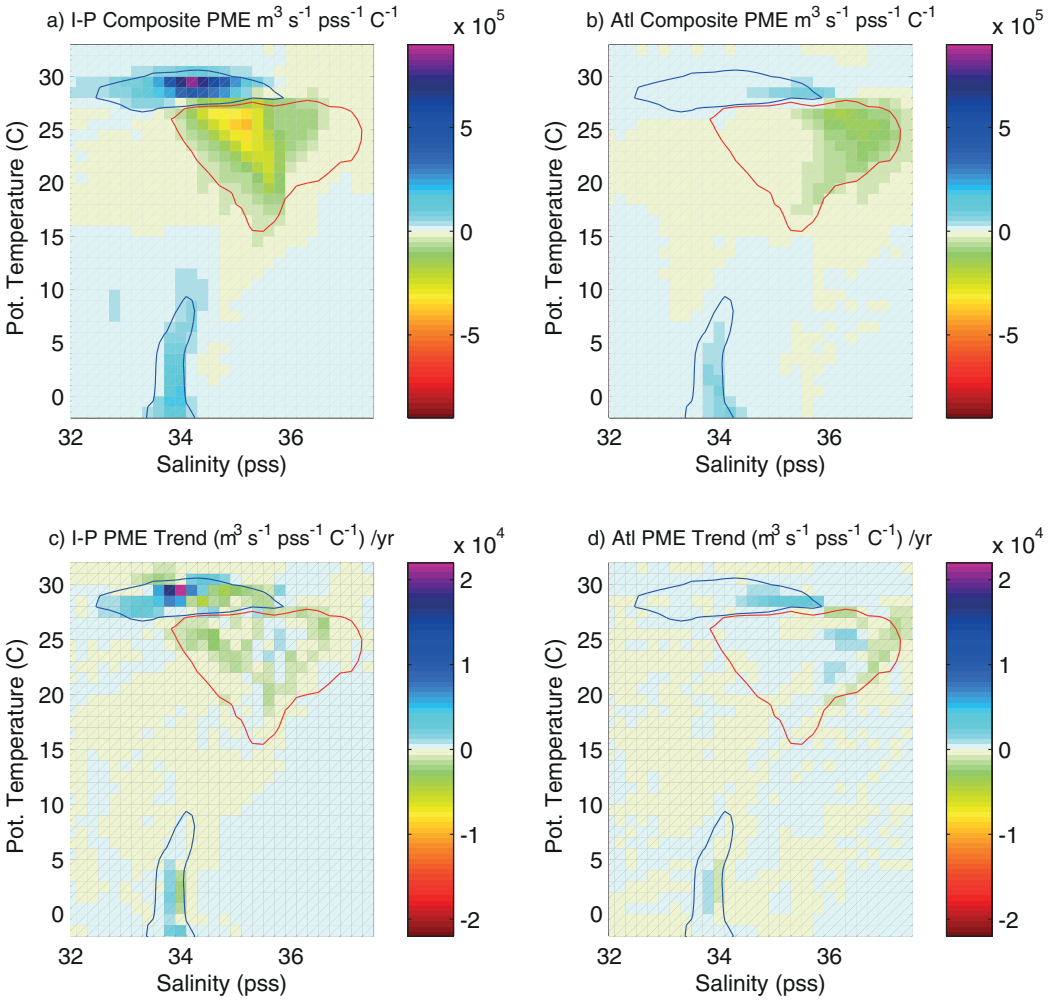

Figure 4. Composites of the four reanalyses for the 1979–2007 mean PME ($m^3\ s^{-1}\ pss^{-1}\ C^{-1}$) in TS space for (a) the Indian and Pacific basins and (b) the Atlantic basin. Figures on the lower panels are the composites of the 4 reanalyses PME trends ($m^3\ s^{-1}\ pss^{-1}\ C^{-1}$/yr) in T-S space for the (c) Indian and Pacific and (d) Atlantic basins. To aid orientation, the mean positions of the main net precipitation and net evaporation cells (as defined by the positive and negative mean $0.5 \times 10^5\ m^3\ s^{-1}\ pss^{-1}\ C^{-1}$ contours, the same as in Figure 2e) are shown as blue and red contours respectively.

the composite trend from the four reanalysis (Figure 2e). In particular, there is an increase in net precipitation in the tropical belt (30°C, 33.0–34.5 pss) and the mid-high latitude net precipitation belt shifts to lower salinities. However, in contrast to the reanalysis composite trend, the 29 year H1PC trend shows a increase in net evaporation near the warmest part of the net evaporative cell (28°C, 34–36 pss) and a decrease over much of the rest of the cell. The 29 year trend in the control run (Figure 5d) does have a similar pattern to H1PC, albeit with a weaker magnitude. This suggests that that a proportion of the 29 year H1PC trend may be associated with drift in the model.

The 140 year trend of PME in the H1PC run also displays some similarities to the composite trend from the four reanalyses (Figure 2e). An increase in net precipitation occurs on the warm flank of the tropical cell (31–33°C, 33.2–34.2 pss) and the mid-high latitude net precipitation belt cell strengthens. However, unlike the reanalysis composite trend, the 140 year H1PC trend shows a increase in net evaporation near the coolest, most saline part of the net precipitation cell and the warmest part of the net evaporative cell (29–31°C, 33.5–35 pss). Most of the subtropical cell displays a significant decrease in net evaporation. The 140 year trend in the control run (Figure 5f) is negligible suggesting the PME trends noted in Figure 5e) are not associated with model drift.

To further understand observed and projected trends in PME we consider the extent to which the trends affect the (T-S) location of each of the 3 main cells shown in Figure 1. Having fitted the linear trend to the

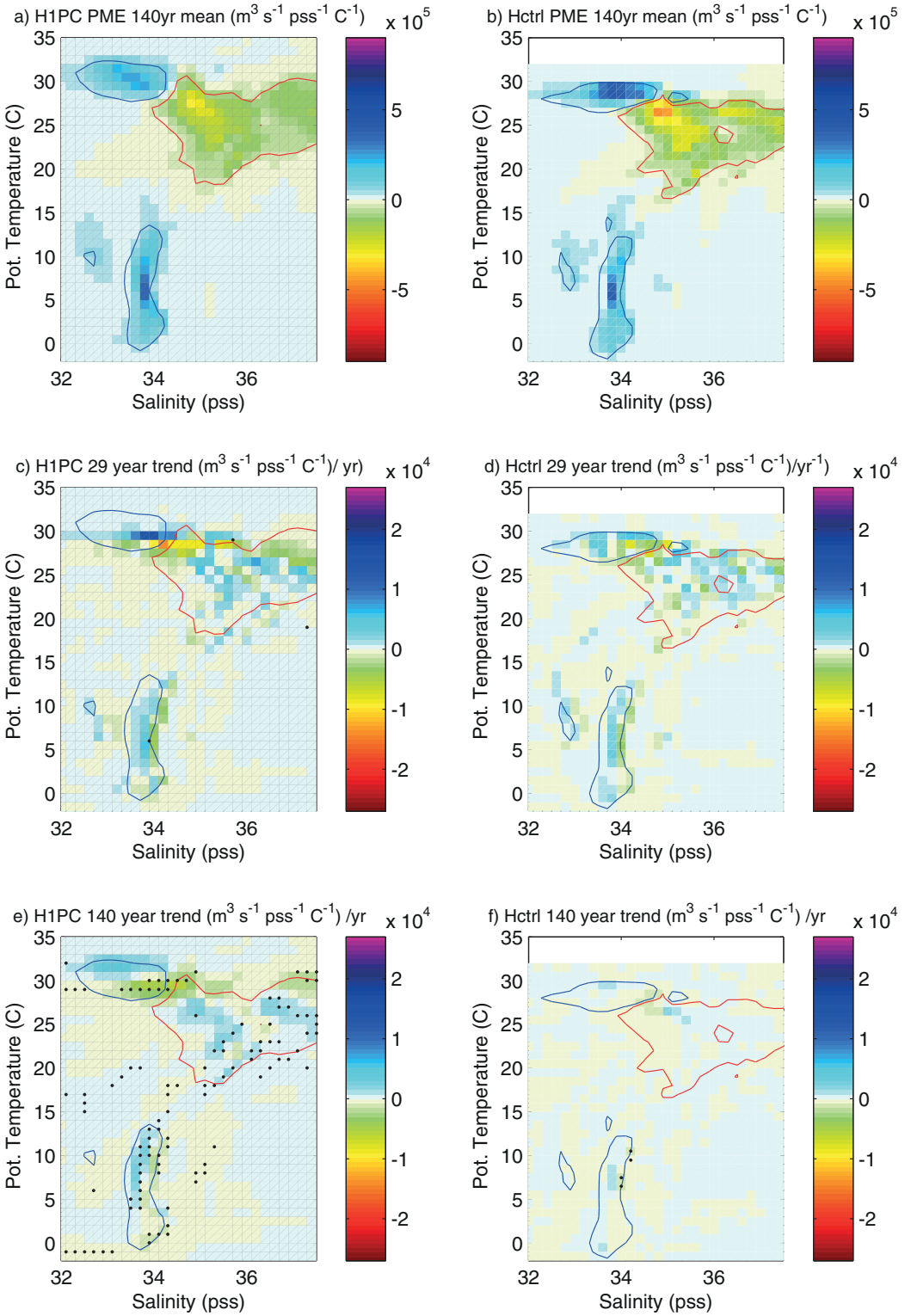

Figure 5. Mean PME ($m^3\ s^{-1}\ pss^{-1}\ C^{-1}$) in T-S space in HadGEM3 (a) 140 years run of 1PC run; (b) 140 years of present day control run. Trends in PME ($m^3\ s^{-1}\ pss^{-1}\ C^{-1}$/yr) (c) first 29 years of the H1PC, (d) first 29 years of Hctrl, (e) 140 years of H1PC, and (f) 140 years of Hctrl. Black dots denote where half the change between the start and end of the run segment associated with a linear trend that is greater than 2 standard deviations of the detrended time series. The mean positions of the main net precipitation and net evaporation cells (as defined by the positive and negative mean $0.5 \times 10^5\ m^3\ s^{-1}\ pss^{-1}\ C^{-1}$ contours) are shown as blue and red contours respectively.

annual PME fields, the location of the main cells for the start and end years of the trend are plotted (Figure 6). Specifically, net precipitation and net evaporation cells are defined by the contours of plus and minus 1.6 × 10 m s^{-1} pss^{-1} C^{-1} PME respectively. PME contours for years 1 and years 29 are plotted (Figure 6). Three of the four reanalyses (NCEP2, JRA and MERRA) show a broadening of the tropical cell, predominantly toward lower salinities. Three of the reanalyses (NCEP2, JRA and ERA-I) show an expansion of the subtropical cell, although not in a consistent manner. Expansion of the high latitude precipitation cell is evident in two of the four reanalyses examined here. We note here that the shifts in the cells recorded in the reanalyses are greater than that shown over the same time period of the H1PC (Figure 6e). The greater strength of the changes in the reanalyses over this period compared to H1PC found in the present study is consistent with earlier studies that note observed freshwater flux trends are greater than those projected in other climate models [e.g., *Zhang et al*., 2007; *Allan and Soden*, 2008]. The extent that this difference reflects inadequacy in the observations or the model projections remains unresolved [e.g., *Liepert and Previdi*, 2009, *Durack et al*., 2012] and requires further study. Considering the climate model over the full length (140 years) of the 1% run rather than the shorter 29 year period examined so far, reveals much larger shifts in all three cells, with all three of them moving to lower salinity, and unlike in the reanalyses, to higher temperatures (Figure 6f).

A useful way of examining changes in the three main precipitation cells is to condense them into changes in temperature classes. When examined in this manner the tropical net precipitation cell is at surface temperatures greater than 27.5°C, the net evaporative cell is between 15 and 27.5°C and the mid-high latitude net precipitation cell is at temperatures less than 15°C (Figure 7a). We can formally partition the PME into three cells: (i) PME^{+warm} (i.e., tropical net precipitation) where there is positive net precipitation at temperatures greater than 22° C, (ii) PME^{-ve}, where there is negative mean PME, and (iii) PME^{+cold}, where there is positive net precipitation at temperatures less than 22° C. Although the vast majority of PME^{+warm} is at temperatures greater than 27.5°C, utilizing the 22°C isotherm to delineate warm from cold net precipitation allows an unambiguous definition of the three cells. There is consistency in the nature of this decomposition between the reanalyses; in all cases there is a greater proportion of net precipitation in the warm region. Specifically, the warm net precipitation is on average 1.5 times greater than the cold net precipitation with the range being between 1.3 and 1.8. This is in contrast to the Hctrl and H1PC where cold PME is 1.6 and 3.1 times greater than warm PME (Figure 7b).

In this framework, in three out of the four reanalyses (NCEP2, JRA, MERRA), the precipitation trends for 1979–2007 show increased net precipitation in the tropics and increased net evaporation in the subtropics (Figures 7c and 7d). While it does not necessarily follow that these changes can be attributed to global warming, the changes are at least consistent with global warming projections that typically reveal wet regions get wetter and dry regions get drier [*Durack and Wijffels*, 2010] (hereafter WGW). We note however, that fully estimating changes in the closed water cycle requires the run-off and ice-melt terms not analyzed here. The fourth reanalysis, ERA, shows a negative trend in all three regions. There is no agreement as to the change in strength of the mid-high latitude net precipitation cell with two of the reanalyses showing increasing precipitation and two showing decreasing precipitation (Figure 7e). If we ignore the effects of run-off and ice-melt then the flux of water from net evaporation regions to net precipitation regions should equal (a) the sum of PME^{+cold} and PME^{+warm} or (b) the absolute value of PME^{-ve}. We therefore estimate the strength of the water cycle as the mean of our estimate of (a) and (b). The results show that all four of the reanalyses have an increasing trend in this estimate of the water cycle strength (Figure7f). The mean (standard deviation) trend for the four reanalyses is 0.018 (± 0.013) Sv/yr or the equivalent of a 14% increase over the 29 year period (with the range being between 2 and 30% increase over the 29 year period). The 140 year run of the H1PC also shows increasing precipitation in the tropical (8.4×10^{-4} Sv/yr, with a standard error of 1.4×10^{-4} Sv/yr) and mid-high latitude (1.4×10^{-3} Sv/yr, with a standard error of 0.06×10^{-3} Sv/yr) precipitation cells and increasing evaporation (-4.3×10^{-3}, Sv/yr, with a standard error of 1.7×10^{-3} Sv/yr) in the subtropics consistent with the WGW understanding of projected hydrological cycle changes. However, the size of the estimated trend in the model flux from net evaporation to net precipitation regions is only about 20% of the mean 1979–2007 reanalyses trend (Figure 7f). This highlights the strength of the PME changes in the reanalyses during the study period.

Finally in this section, we condense the T-S analysis into a single salinity coordinate to examine the mean strength and trend of the water cycle as depicted from the atmospheric reanalyses. In the mean (Figure 8a), the positive net precipitation peaks at approximately (3.0 Sv pss^{-1}) in fresher water (34 pss) and negative

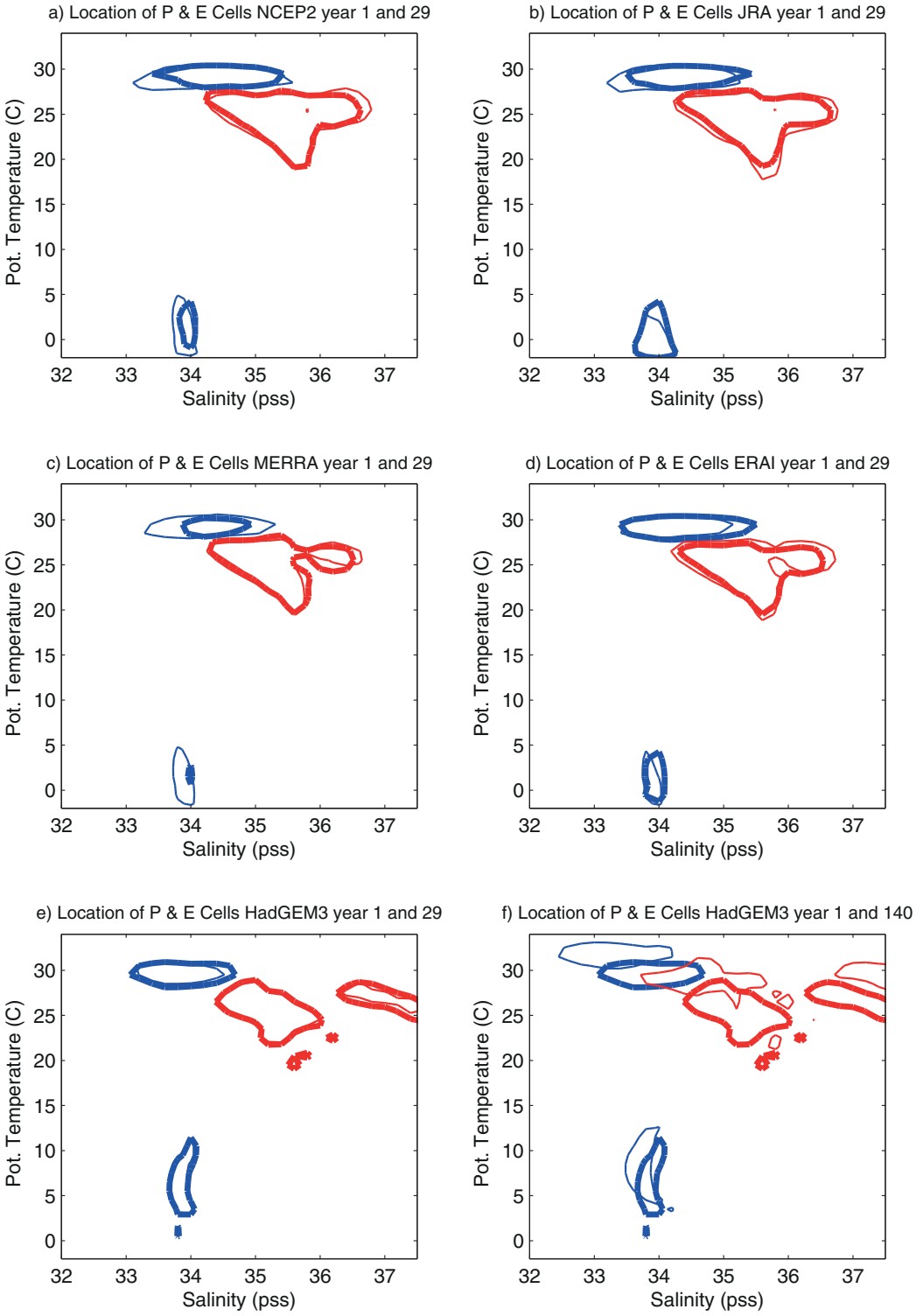

Figure 6. Change between 1979 and 2007 associated only with the linear trend in location of the main net precipitation (blue contours) and evaporation (red contours) regions in (a) NCEP 2; (b) JRA; (c) MERRA; and (d) ERA-I. Location of the net precipitation and evaporation regions for (e) year 1 and year 29 and (f) year 1 and year 140 of the H1PC. In all plots, net precipitation and net evaporation are defined by the contours of plus and minus 1.6×10^5 m^3 s^{-1} pss^{-1} C^{-1} PME respectively. The original location is denoted as a thick contour and the later location as a thin contour.

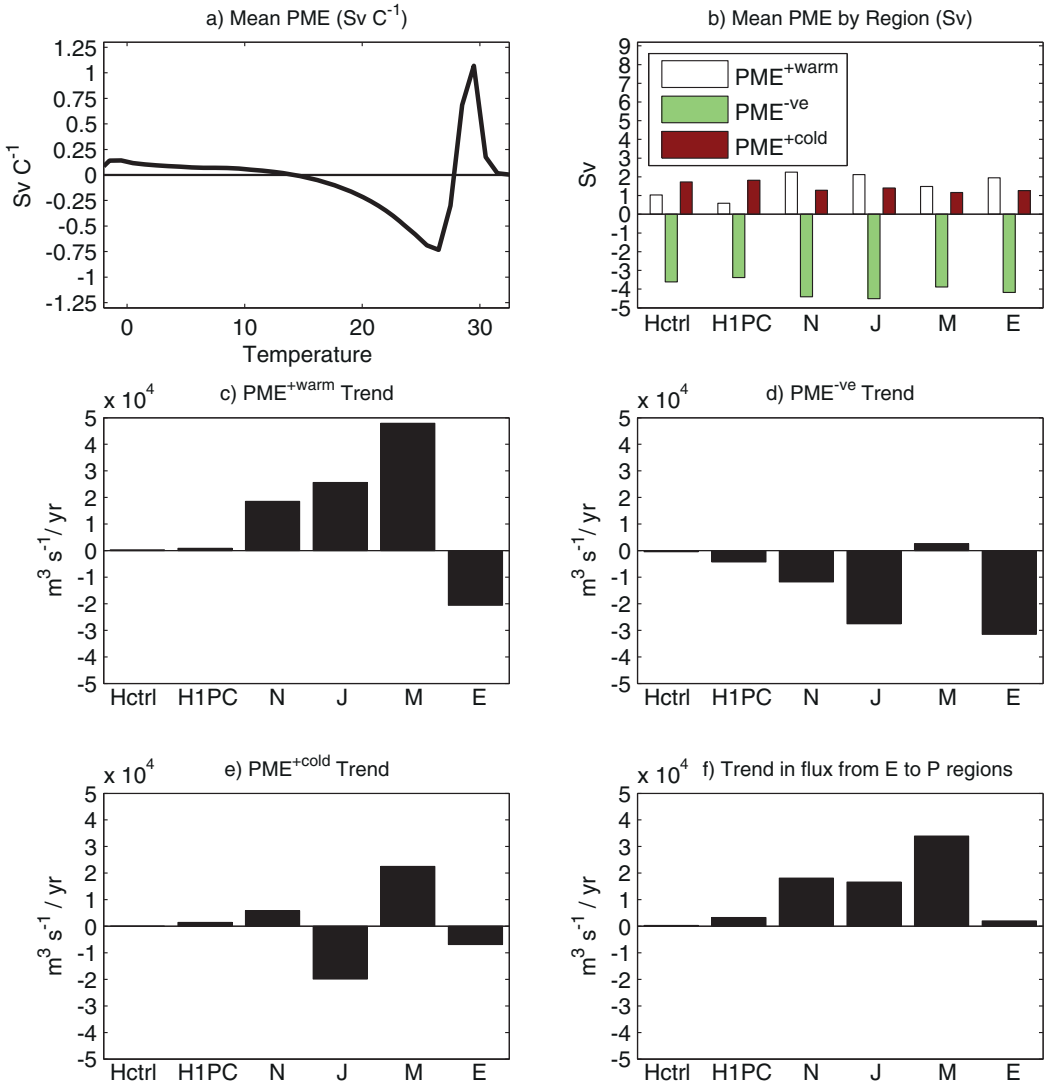

Figure 7. (a) Mean PME (Sv C^{-1}) in 1° temperature bins (integrated across all salinities) of the four atmospheric reanalysis. (b) Mean PME (Sv) by region: PME^{+warm} (region of mean net precipitation warmer than 22°C); PME^{-ve} (region of mean net evaporation) and PME^{+cold} (region of mean net precipitation colder than 22°C). PME trends (Sv/yr) for the Hctrl and H1PC (140 years) and the four reanalyses (29 years) for Figure 7a PME^{+warm}, PME^{-ve} and PME^{+cold}, (f) the flux from net evaporation to net precipitation regions (estimated as the mean of the total precipitation and evaporation trends).

net precipitation peaks (−2.0 Sv pss^{-1}) at 35.5 pss. The peaks from the runs of HadGEM3 are offset slightly to lower salinities. Decomposing the PME (as a function of salinity) into PME^{+warm}, PME^{+cold} and PME^{-ve} reveals the PME^{+cold} peak is stronger and over a narrower salinity range than PME^{+warm} (Figures 8c and 8g). To examine the effect that the linear trends have on the salinity distribution of PME, we use the same approach as in Figure 4. A linear trend is fitted to the annual PME salinity distributions and values for the start and end years of the trend are plotted in Figure 8b. In the mean, the atmospheric reanalyses (black lines Figure 8b) experienced a strengthening and a shift toward lower salinities. The decomposition of the trend (Figures 8d, 8f, and 8h) reveals that this change occurs largely due to changes in the PME^{+warm} regions with relatively little change in the other regions. This is in contrast to the H1PC where a shift toward lower salinities is mainly associated with changes in the PME^{+cold} region and there is a clear broadening of PME in the evaporative region.

Summarizing the analysis of PME trends, the average of the four atmospheric reanalyses (Figure 2e) indicates an increase in precipitation between 1979 and 2007 in the fresher region of tropical net precipitation and an increase in net evaporation in the subtropical cell. This increase is consistent with the WGW view.

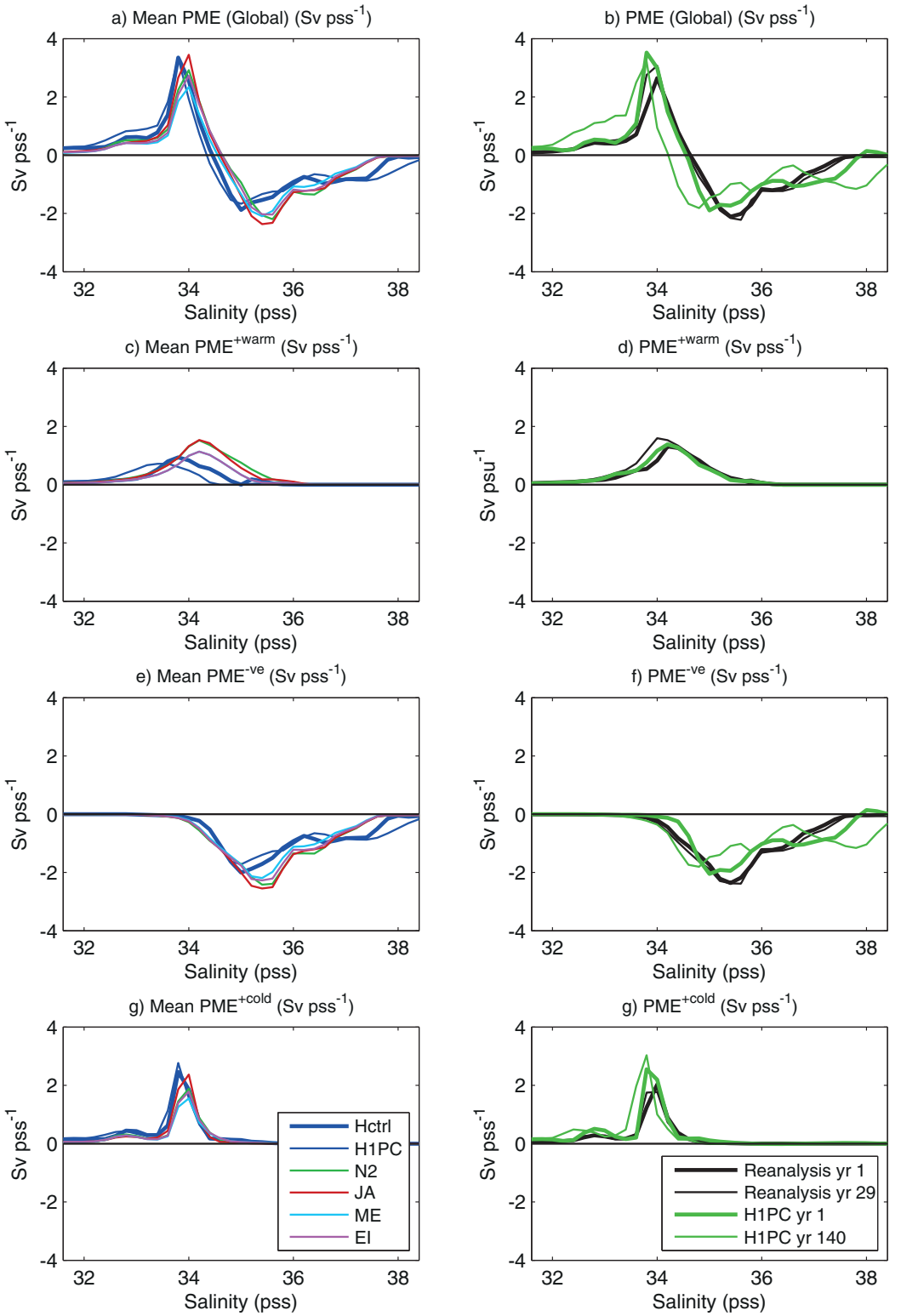

Figure 8. (a) Mean global ocean PME (Sv pss^{-1}) as a function of surface salinity for the 4 atmospheric reanalysis and the Hctrl and H1PC runs of HadGEM3; (c, e, and g) the same for the PME^{+warm}, PME^{-ve}, PME^{+cold} sectors respectively. (b) Change between 1979 (thick black line) and 2007 (thin black line) associated only with the linear trend in PME as a function of salinity in the mean of the four reanalyses. Also shown is the same for year 1 (green line) and year 140 (thin green line) of H1PC. (d, f, and g) Same as Figure 8a but for the PME^{+warm}, PME^{-ve}, and PME^{+cold} sectors respectively.

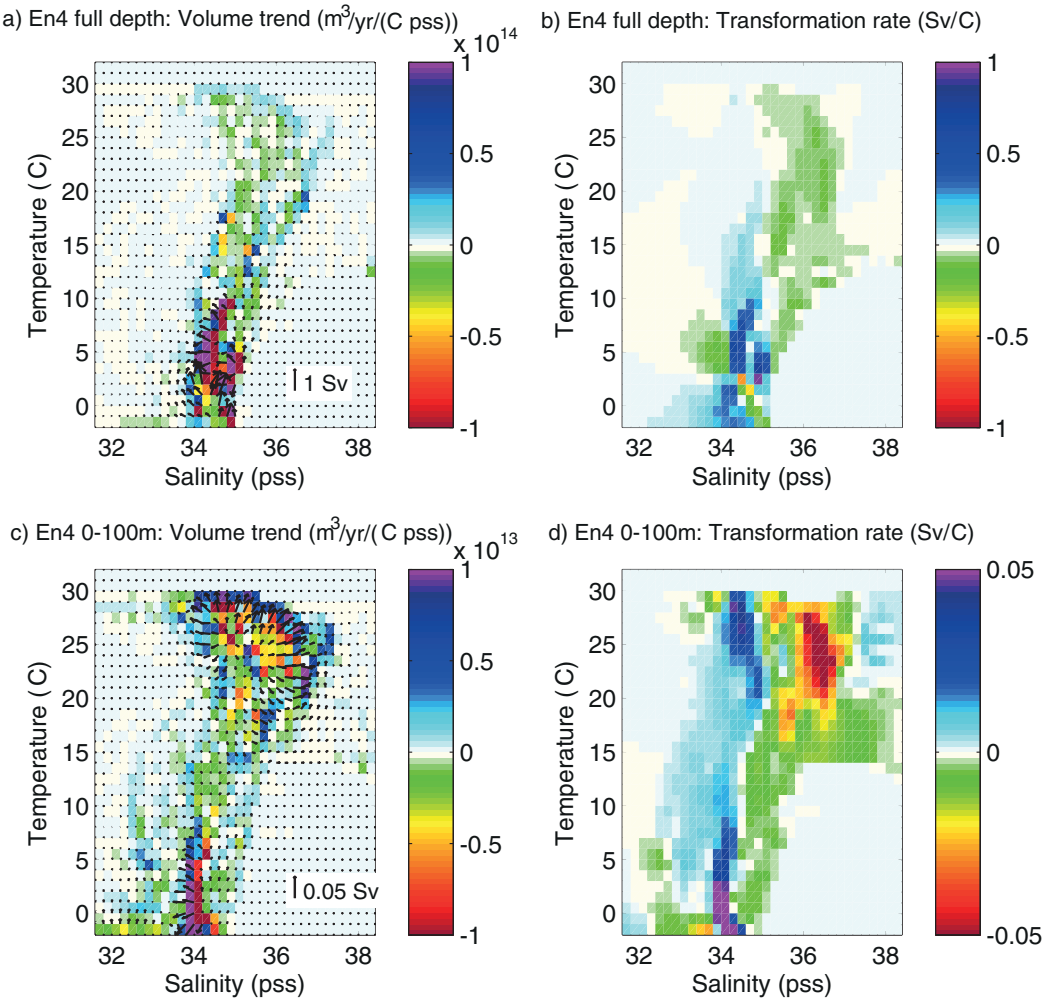

Figure 9. (a) Total change in volume of the global ocean occupied in T-S bins based on EN4 observations 1979–2007 ($m^3\ C^{-1}\ pss^{-1}/yr$). Vectors indicate dia-surface transformations (Sv) in T-S space over the whole period. (b) The x component of the dia-surface transformation, which indicate transformations across isohalines ($Sv\ C^{-1}$). (c and d) Same as Figures 9a and 9b but for top 100 m of Global Ocean only.

There is also a tendency for the tropical cell to expand toward lower salinities. The reanalyses differ as to the sign of mid-high latitude net precipitation changes. However, the shift of the net precipitation cell toward lower salinities is a more robust result. All four of the reanalyses demonstrate a strengthening of the hydrological cycle, with the mean rate being 0.018 Sv/yr (1.8×10^4 ($m^3\ s^{-1}$)/yr. This increase is consistent with the WGW view. The H1PC also demonstrates an increase in the strength of the hydrological cycle (Figure 7f). However, the H1PC trends are smaller relative to the 1979–2007 reanalysis. The most marked change in PME in H1PC is the shift of all the three main cells to warmer temperatures and lower salinities.

4.2. Changing Global Ocean Water Mass Characteristics

We now examine the trends in the T-S distribution of the global ocean water masses. In particular, we consider if water masses display an imprint of PME trends and whether these are consistent with those examined in the reanalysis products. Figures 9a and 9c. show the 1979–2007 trend in the volumetric distribution for each T-S bin in the full depth and top 100m of the Global Ocean respectively. Vectors show associated total dia-surface (dia-thermal/dia-haline) transformations solved for by using the 1979–2007 volumetric trend in equation (2). These dia-surface transformations have in units of Sv ($Sv=10^6\ m^3/s$) [*Evans et al.*, 2014]. In addition we plot the dia-haline transformations for full depth and the top 100 m in Figures 9b and 9d) respectively divided by the temperature interval and reference salinity (i.e., $-G_S/\Delta TS_0$; where $S_0=35pss$).

These plot the transformation of fresher water across the isohaline, in the same units as PME and so that positive values represent a freshening and negative values represent salinification.

We consider the full depth volume change in two ranges. Firstly at temperatures greater than 15°C, there is a broader area of divergence. That is to say there is an area (16–28°C, 34.6–36.0 pss) where volume decreases at the expense of increases in the adjacent regions (lower salinities, higher salinities and higher temperatures). At lower temperatures a more spatially complex pattern exists with large increases and decreases occurring within relatively close T-S vicinity. This pattern may be complicated by significant changes in non-PME freshwater forcing such as ice-melt and river run-off. Despite this complex volume change pattern, and with the exception of some more subtle features at low salinities, for example, a negative value at around 5°C and 34 pss, the transformation across isohalines shows a very simple signal (Figure 9b). Broadly speaking at salinities lower than 35.0 pss it shows water being transformed from higher to lower salinities and at salinities higher than 35.0 water being transformed from lower to higher salinities. The general pattern of water masses transformation is consistent with a broadening of the ocean salinity distribution associated with WGW [*Zika et al*., 2015], however this analysis reveals further structure to the broadening. This broadening is evident across a wide temperature range from −2°C to 20°C, with the exception being between 3°C and 7°C, where there is some convergence (in salinity space) around 34.5pss. Water with temperatures lower than 3°C is typically fresher than the global average, and the predominant trend is for this water to freshen further and shift the distribution to lower salinities as opposed to broaden to low and high salinities.

Although surface waters are affected by upwelling, downwelling, mixing and advection, it is expected that near surface changes in the T-S distribution may contain a signal of changes in PME described earlier (Figure 2e). We now examine if this is the case by looking at the volumetric changes (and dia-tracer transformations) of the upper 100 m of the global ocean (Figures 9c and 9d). Considering first, the observations at mid-high latitude regions (predominantly the Southern Ocean), at temperatures lower than 10°C, the volume of water at less than 34 pss increases at the expense of water greater than 34.5 pss. This is consistent with the increase in reanalysis precipitation at salinities less than 34.0 (Figure 2e), so while not discounting a role for ice-melt, this suggests that over this period increases in PME fluxes helped shift the Southern Ocean to a less saline distribution. Further analysis is required to decompose the relative contributions of sea-ice and PME to Southern Ocean freshening [*Durack and Wijffels*, 2010; *Haumann et al*., 2016].

Turning our attention to the subtropics, dia-surface transformations indicate a divergence in water mass properties, with the more saline waters, in the T-S range typical of in the Atlantic Ocean (e.g., 36.0–36.7 pss, 26–28°C) becoming warmer and more saline and the fresher waters with T-S values typical of the Indo-Pacific (e.g., 34.2 pss, 25°C) becoming warmer and less saline. Analysing the salinity trends in the subtropical gyres, *Melzer and Subrahmanyam* [2015] also found the Atlantic subtropical gyres becoming more saline between 1950 and 2010. The observed salinification of the Atlantic is in accord with the consistent, albeit not very strong, increase in net evaporation across the reanalyses (Figure 7d). However, the freshening in the Pacific, appears to be in contrast with the reanalyses surface fluxes that show increased net evaporation. Examination of a 1950–2010 time series of Pacific subtropical gyre salinity [*Melzer and Subrahmanyam*, 2015, Figure 4] indicates that although the 60 year trend has been one of increased salinity, 1979–2007 exhibited a slight decrease.

The final T-S area we consider is the tropics, in particular the typically precipitation dominated region (i.e., greater than 28°C in the reanalyses/observations). This region is marked by an increase in the volume of the warmest waters (i.e., around 29°C), particularly between 34 and 35.5 pss, that is in the Pacific and the Indian Oceans To a certain extent both these changes are expected by the location of the increase in tropical precipitation shown in the reanalysis (Figure 2). These changes are also consistent with the PME^{+warm} cell moving to higher temperatures as in H1PC (Figure 6f).

Finally in this section, it is noted that a signature of an increasing hydrological cycle is a broadening of the salinity distribution [*Zika et al*., 2015]. This increase in volume at high and low salinities at the expense of that at intermediate salinities is manifest by the clear dipole structure in the cross isohaline transformation rate (Figures 9b and 9d)). Similar changes in salinity structure are also found in H1PC (Figure 10). In particular in the top 100 m (Figure 10d), the dipole structure is evident from −2°C to 29°C. At temperatures warmer than 29°C, near 33.6 pss, the strong warming leads an initially positive PME region to become negative

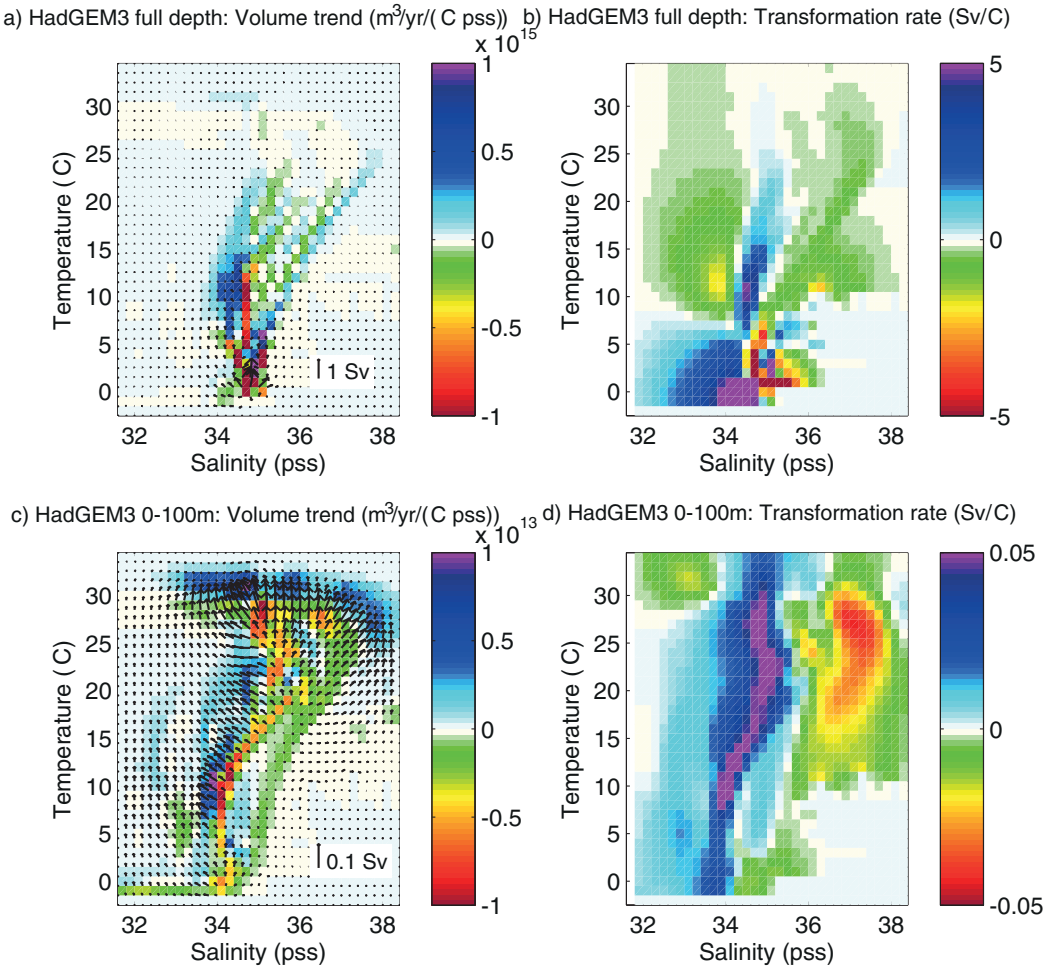

Figure 10. (a) Total change in volume of the global ocean occupied in T-S bins based on 140years of H1PC ($m^3\ C^{-1}\ pss^{-1}/yr$). Vectors indicate dia-surface transformations (Sv) in T-S space over the whole period. (b) The x component of the dia-surface transformation, which indicate transformations across isohalines ($Sv\ C^{-1}$). (c and d) Same as Figure 10a and 10b but for top 100 m of Global Ocean only.

(Figure 6f), resulting in a more complex redistribution of water masses. Similar to the top 100m case, the full-depth volume trend (Figure 10a) shows a large temperature range (between 5°C and 24°C) where volume decreases are flanked (i.e., at higher and lower salinities) by volume increases (i.e., a broadening of the salinity distribution). The corresponding cross-isohaline transformation rate (Figure 10b) exhibits a similar dipole structure to that observed 1979–2007 (Figure 9b), although a noticeable difference is that the observed negative transformation rate near 33.5pss and 5°C, has a greater magnitude, is located at a higher temperature and covers a broader area in H1PC. However, in general, a comparison of Figures 9b, 9d, 10b, and 10d indicate the observed water mass changes between 1979 and 2007 have strong similarities to changes anticipated under HadGEM3's depiction of a global warming scenario. These changes and in particular the broadening of the salinity distribution are consistent with the intensification of the hydrological cycle between 1979 and 2007 found in the analyses of four diverse atmospheric reanalyses (section 4.1).

5. Conclusions

A T-S based analysis of PME trends has been carried out for the period 1979–2007 using multiple atmospheric reanalysis data sets (ERAI, JRA, MERRA, and NCEP2). The advantages of such an approach are that it simplifies the spatial variability and provides a more instructive link between PME and changes in water mass T-S properties which will ultimately affect the Global Thermohaline Circulation. During the period 1979–2007, the reanalyses consistently exhibit three distinct PME trends. We have sought to understand

these changes in the context of observed changes in ocean T-S distribution and the long term PME associated with Global Warming according to the HadGEM3 climate model.

First, at temperatures less than 10°C, there is a shift in the main net precipitation belt toward lower salinities (below 34 pss). This corresponds to a similar shift toward more (less) volume of water at salinities less (greater) than 34 pss in the observations. In geographical coordinates this trend is manifest as freshening of the Southern Ocean. The trends noted in the atmospheric reanalysis and the ocean observations are similar to those in a 1% pa increase CO2 run of the HadGEM3 climate model, with the caveat that in the climate model, the net precipitation cell and the corresponding T-S distribution also shift to warmer temperatures.

Second, in tropical regions, specifically at temperatures greater than 27°C and salinities less than 34.5 pss, the reanalyses display an increase in net precipitation and a tendency for the net precipitation cell to move to lower salinities. This net precipitation increase is consistent with the increased upper ocean water mass volume in this T-S range. However, the observed tropical T-S distribution also shows a shift toward warmer temperatures. The climate model showed only a slight increase in net precipitation, but a marked shift to warmer temperatures and lower salinities.

The third PME change indicated from the reanalyses is an increase in net evaporation in the subtropical region between 15°C and 27°C. Although this is a less robust signal from the atmospheric reanalyses, confidence that such a change is real is strengthened by the observed shift toward higher salinities in the upper 100m of the ocean. The subtropical salinity changes are consistent with the global warming signal in HadGEM3, which shows the Pacific subtropical precipitation cell freshening and the Atlantic subtropical cell moving to higher salinities.

We have shown that the trends described above are robust across multiple reanalyses and note here that this common behaviour has not previously been recognized. A caveat is required since, as discussed in section 4.1, the temporally varying observing network has the potential to introduce unphysical temporal trends [*Fasullo*, 2012]. With this in mind we note that there are some differences in the reanalyses trend patterns when different time periods were considered (Figures 2 and 3). However, the overall level of consensus is strong and the resulting composite pattern shows the main features expected from an amplification of the water cycle. This is particularly the case for T greater than about 13 °C and this is consistent with increases in tropical precipitation and subtropical evaporation found in blended (i.e., observations combined with reanalysis) products [*Skliris et al*., 2014].

In summary, we stress that our analysis was conducted with a diverse set of atmospheric reanalyses and that the common PME trends found across these reanalyses are supported by a high degree of consistency with independent observations of changes in the T-S distribution of the upper ocean waters. Furthermore, the sense of the observed changes is consistent with the global warming signal in H1PC. However, the relatively large magnitude of the reanalysis trends relative to H1PC, indicates that over the relatively short period 1979–2007, some of the trends are likely inflated by interdecadal variability as opposed to a response to a centennial scale global warming signal. Nonetheless, the results support the contention that 1979–2007 was a period of intensification of the hydrological cycle which resulted in a broadening of the salinity distribution of the Global Ocean. The analysis further reveals that while this broadening was focussed across tropical/subtropical temperatures, at lower temperatures there was a substantial volumetric water mass distribution shift to lower salinities, as opposed to broadening to both lower and higher salinities. The results suggest this may have been caused by ocean processes redistributing high temperature freshening to lower temperatures.

Acknowledgments
JPG, SAJ, JDZ and NS are funded by the Natural Environment Research Council Project CLAW (Climate-Scale Analysis of Air and Water masses), NE/K012932/1. EN4 data are provided by the UK Met Office (http://www.metoffice.gov.uk/hadobs/en4/). The NCEP2, JRA, MERRA, and ERA-I reanalyses are available through the reanalyses.org portal.

References

Adler, R. F., G. Gu, J.-J. Wang, G. J. Huffman, S. Curtis, and D. Bolvin (2008), Relationships between global precipitation and surface temperature on interannual and longer timescales (1979 – 2006), *J. Geophys. Res.*, *113*, D22104, doi:10.1029/2008JD010536.

Allan, R. P., and B. J. Soden (2008), Atmospheric warming and the amplification of precipitation extremes, *Science*, *321*, 1481–1484, doi:10.1126/science.1160787.

Allan, R. P., B. J. Soden, V. O. John, W. Ingram, and P. Good (2010), Current changes in tropical precipitation, *Environ. Res. Lett.*, *5*, 025205, doi:10.1088/1748-9326/5/2/025205.

Bernie, D. J., E. Guilyardi, G. Madec, J. M. Slingo, S. J. Woolnough, and J. Cole (2008), Impact of resolving the diurnal cycle in an ocean atmosphere GCM. Part 2: A diurnally coupled CGCM, *Clim. Dyn.*, *31*(7–8), 909–925, doi:10.1007/s00382-008-0429-z.

Dee, D. P., et al. (2011), The ERA-Interim reanalysis: Configuration and performance of the data assimilation system, *Q. J. R. Meteorol. Soc.*, *137*, 553–597, doi:10.1002/qj.828.

Durack, P. J., and S. E. Wijffels (2010), Fifty-year trends in global ocean salinities and their relationship to broad-scale warming, *J. Clim.*, *23*, 4342–4362, doi:10.1175/2010JC13377.1.
Durack, P. J., S. E. Wijffels, and R. J. Matear (2012), Ocean salinities reveal strong global water cycle intensification during 1950 to 2000, *Science*, *336*, 455–458, doi:10.1126/science.1212222.
Evans, D. G., J. D. Zika, A. C. Naveira-Garabato, and A. J. G. Nurser (2014), The imprint of Southern Ocean overturning on seasonal water mass variability in Drake Passage, *J. Geophys. Res. Oceans*, *119*, 7987–8010, doi:10.1002/2014JC010097.
Fasullo, J. (2012), A Mechanism for land-ocean in global monsoon trends in a warming climate, *Clim. Dyn.*, *39*, 1137–1147, doi:10.1007/s00382-01101270-3.
Fiorino, M. (2004), A multi-decadal daily sea surface temperature and sea ice concentration data set for the ERA-40 reanalysis, *ERA-40 Project Report Series* No. 12, ECMWF: Reading, U. K.
Gao, S., L. S. Chiu, and C. L. Shie (2013), Trends and variations of ocean surface latent heat flux: Results from GSSTF2c data set, *Geophys. Res. Lett.*, *40*, 380–385, doi:10.1029/2012GL054620.
Gent, P. R., and J. C. McWilliams (1990), Isopycnal mixing in ocean circulation models, *J. Phys. Oceanogr.*, *20*, 150–155.
Good, S. A., M. J. Martin, N. A. Rayner (2013), EN4: Quality controlled ocean temperature and salinity profiles and monthly objective analyses with uncertainty estimates, *J. Geophys. Res. Oceans*, *118*, 6704–6716, doi:10.1002/2013JC009067.
Gouretski, V., and F. Reseghetti (2010), On depth and temperature biases in bathythermograph data: Development of a new correction scheme based on analysis of a global ocean database, *Deep Sea Res., Part I*, *57*, 812–833, doi:10.1016/j.dsr.2010.03.011.
Grist, J. P., S. A. Josey, R. Marsh, Y.-O. Kwon, R. J. Bingham, and A. T. Blaker (2014), The Surface-forced overturning of the North Atlantic: Estimates from modern era atmospheric reanalysis datasets, *J. Clim.*, *27*, 3596–3618, doi:10.1175/JCLI-D-13-00070.1.
Groeskamp, S., J. D. Zika, T. J. McDougall, B. M. Sloyan, and F. Laliberté (2014), The representation of Ocean Circulation and Variability in Thermodynamic Coordinates, *J. Phys. Oceanogr.*, 1735–1750, doi:10.1175/JPO-D-13-0213.
Gu, G., R. F. Adler, and G. J. Huffman (2016), Long-term changes/trends in surface temperature and precipitation during the satellite era (1979-2012), *Clim. Dyn.*, *46*, 1091–1105, doi:10.1007/s00382-015-2634-x.
HadGEM2 Development Team (2011), The HadGEM2 family of Met Office Unified Model climate configurations, *Geosci. Model Dev.*, *4*, 723–757, doi:10.5194/gmd-4-723-2011.
Haumann, F. A., N. Gruber, M. Münnich, I. Frenger, and S. Kern (2016), Sea-ice transport driving Southern Ocean salinity and its recent trends, *Nature*, *537*, 89–92, doi:10.1038/nature1910.
Held, I. M., and B. J. Soden (2006), Robust responses of the hydrological cycle to global warming, *J. Clim.*, *19*, 5686–5699.
Hewitt, H. T., D. Copsey, I. D. Culverwell, C. M. Harris, R. S. R. Hill, A. B. Keen, A. J. McLaren, and E. C. Hunke (2011), Design and implementation of the infrastructure of HadGEM3: The next-generation Met Office climate modelling system, *Geosci. Model Dev.*, *4*, 223–253, doi:10.5194/gmd-4-223-2011.
Hieronymus, M., J. Nilsson, and J. Nycander (2014), Water mass transformation in salinity–temperature space, *J. Phys. Oceanogr.*, *44*, 2547–2568.
Hunke, E. C., and W. H. Lipscomb (2010), CICE: The Los Alamos Sea Ice Model, documentation and software user's manual. Version 4.1, *Tech. Rep. LA-CC- 06-012*, Los Alamos Natl. Lab., Los Alamos, N. M. [Available at http://oceans11.lanl.gov/trac/CICE.]
Ineson, S., and A. A. Scaife (2009), The role of the stratosphere in the European climate response to El Nino, *Nat. Geosci.*, *2*(1), 32–36, doi:10.1038/ngeo381.
Ishii, M., A. Shouji, S. Sugimoto, and T. Matsumoto (2005), Objective Analyses of sea-surface temperature and marine meteorological variables for the 20th Century Using ICOADS and the KOBE Collection, *Intl. J. Climatology*, *25*, 865–879.
Jackson, L. R. Kahana, T. Graham, M. A. Ringer, T. Woolings, J. V. Mecking and R. A. Wood (2015), Global and European climate impacts of a slowdown of the AMOC in a high resolution GCM, *Clim. Dyn.*, *45*, 3299–3316, doi:10.1007/s00382-015-2540-2.
Josey, S. A., and R. Marsh (2005), Surface freshwater flux variability and recent freshening of the North Atlantic in the eastern subpolar gyre, *J. Geophys. Res.*, *110*, C05008, doi:10.1029/2004JC002521.
Kanamitsu, M., W. Ebisuzaki, J. Woollen, S.-K. Yang, J. J. Hnilo, M. Fiorino, and G. L. Potter (2002), NCEP-DEO AMIP-II Reanalysis (R-2), *Bull. Am. Meteorol. Soc.*, *83*, 1631–1643, doi:10.1175/BAMS-83-11-1631.
Li, G., B. Ren, C. Yang, and J. Zheng (2011), Revisiting the trend of the tropical and subtropical Pacific surface latent heat flux during 1977–2006, *J. Geophys. Res.*, *116*, D10115, doi:10.1029/2010JD015444.
Liepert, B. G., and M. Previdi (2009), Do models and observations disagree on the rainfall response to global warming, *J. Clim.*, *22*, 3156–3166, doi:10.1175/2008JCLI2472.1.
Madec, G. (2008), NEMO ocean engine, *Note du Pole de Modèlisation 27*, Inst. Pierre-Simon Laplace, Paris, France.
Megann, A., D. Storkey, Y. Aksenov, S. Alderson, D. Calvert, T. Graham, P. Hyder, J. Siddorn, and B. Sinha (2013), Go5.0: The joint NERC-Met Office NEMO global ocean model for use in coupled and forced applications, *Geosci. Model. Dev. Discuss. 6(4)*,5747–5799, doi:10.5194/gmdd-6-5747-2013.
Melzer, B. A., and B. Subrahmanyam, (2015), Investigating decadal changes in sea surface salinity in oceanic subtropical gyres, *Geophys. Res. Lett.*, *42*, 7631–7638, doi:10.1002/2015GL065636.
Onogi, K., et al. (2007), The JRA-25 reanalysis, *J. Meteorol. Soc. Jpn.*, *85*, 369–432.
Reynolds, R. W., N. A. Rayner, T. M. Smith, D. C. Stokes, and W. Wang (2002), An improved in situ and satellite SST analysis for climate, *J. Clim.*, *15*, 1609–1625.
Rienecker, M. M., et al. (2011), MERRA-NASA's modern-era retrospective analysis for research and applications, *J. Clim.*, *24*, 3624–3648, doi:10.1175/JCLI-D-11-00015.1.
Robertson, F. R., M. G. Bosilovich, J. Chen, and T. L. Miller (2011), The effect of satellite observing system changes on MERRA water and energy fluxes, *J. Clim.*, *24*, 5197–5217, doi:10.1175/2011JCLI4227.1
Scaife, A. A., D. Copsey, C. Gordon, C. Harris, T. Hinton, S. Keeley, A. O'Neill, M. Roberts, and K. Williams (2011), Improved Atlantic winter blocking in a climate model, *Geophys. Res. Lett.*, *38*, L23703, doi:10.1029/2011GL049573.
Senior, C. A., et al. (2016), Idealized climate change simulations with a high-resolution physical model: HadGEM3-GC2, *J. Adv. Model. Earth Syst.*, *8*, 813–830, doi:10.1002/2015MS000614.
Seidel, D. J., Q. Fu, W. J. Randel, and T. J. Reichler (2008), Widening of the tropical belt in a changing climate, *Nat. Geosci.*, *1*, 21–24, doi:10.1038/ngeo.2007.38.
Skliris, N., R. Marsh, S. A. Josey, S. A. Good, C. Liu, and R. P. Allan (2014), Salinity changes in the World Ocean since 1950 in relation to changing surface freshwater fluxes, *Clim. Dyn.*, *43*, 709–736, doi:10.1007/s00382-014-2131-7.
Taylor, K. E., D. Williamson, and F. Zwiers (2000), The sea surface temperature and sea-ice concentration boundary conditions for AMIP II simulations, PCMDI Report No. 60, Program for Climate Model Diagnosis and Intercomparison, Lawrence Livermore National Laboratory, 25 pp., Livermore, Calif.

Wentz, F. J., L. Ricciardulli, K. Hilburn, and C. Mears (2007), How much more rain will global warming bring?, *Science*, *317*, 233–235, doi: 10.1126/science.1140746.

Williams, K. D., et al. (2015), The Met Office Global Coupled model 2.0 (GC2) configuration, *Geosci. Model Dev.*, *88*, 1509–1524, doi:10.5194/gmd-88-1509-2015.

Yu, L. (2007), Global variations in oceanic evaporation (1958–2005): The role of the changing wind speed, *J. Clim.*, *20*(21), 5376–5390, doi: 10.1175/2007JCLI1714.1.

Zhang, X., F. W. Zwiers, G. C. Hegerl, F. H. Lambert, N. P. Gillet, S. Solomon, P. A. Stott and T. Nozawa (2007), Detection of human influence on twentieth-century precipitation, *Nature*, *448*, 461–465, doi:10.1038/nature06025.

Zika, J. D., M. H. England, and W. P. Sijp (2014), The ocean circulation in Thermohaline Coordinates, *J. Phys. Oceanogr.*, *42*, 708–724, doi: 10.1175/JPO-D-11-0139.1.

Zika, J. D, N. Skliris, A. J. G. Nurser, S. A. Josey, L. Mudryk, and F. Laliberté (2015), Maintenance and broadening of the ocean's salinity distribution by the water cycle, *J. Clim.*, *28*, 9550–9560, doi:10.1175/JCLI-D-15-0273.1.